Linköping Studies in Science and Technology
Thesis No. 1484

High-temperature degradation of plasma sprayed thermal barrier coating systems

Robert Eriksson

Linköping University
INSTITUTE OF TECHNOLOGY

LIU–TEK–LIC–2011:23

Department of Management and Engineering, Division of Engineering Materials
Linköping University, 581 83, Linköping, Sweden
http://www.liu.se

Linköping, April 2011

Cover:
A fractured thermal barrier coating system, revealing the interfacial thermally grown oxides which consist mainly of Al_2O_3, (the image width is 12.7 µm).

Printed by:
LiU-Tryck, Linköping, Sweden, 2011
ISBN 978-91-7393-165-6
ISSN 0280-7971

Distributed by:
Linköping University
Department of Management and Engineering
581 83, Linköping, Sweden

This document was prepared with LaTeX, April 25, 2011

Abstract

Thermal barrier coating systems (TBCs) are used in gas turbines to prevent high-temperature degradation of metallic materials in the combustor and turbine. One of the main concerns regarding TBCs is poor reliability, and accurate life prediction models are necessary in order to fully utilise the beneficial effects of TBCs. This research project aims at developing deeper understanding of the degradation and failure mechanisms acting on TBCs during high temperature exposure, and to use this knowledge to improve life assessments of TBCs. The present work includes a study on the influence of coating interface morphology on the fatigue life of TBCs and a study on the influence of some different heat treatments on the adhesive properties of TBCs.

The influence of coating interface morphology on fatigue life has been studied both experimentally and by modelling. Large interface roughness has been found experimentally to increase fatigue life of TBCs. The modelling work do, to some extent, capture this behaviour. It is evident, from the study, that interface morphology has a large impact on fatigue life of TBCs.

Three thermal testing methods, that degrade TBCs, have been investigated: isothermal oxidation, furnace cycling and burner rig test. The degraded TBCs have been evaluated by adhesion tests and microscopy. The adhesion of TBCs has been found to depend on heat treatment type and length. Cyclic heat treatments, (furnace cycling and burner rig test), lower the adhesion of TBCs while isothermal oxidation increases adhesion. The fracture surfaces from the adhesion tests reveal that failure strongly depends on the pre-existing defects in the TBC.

Contents

Nomenclature

APS	air plasma spray
BC	bond coat
BRT	burner rig test
CTE	coefficient of thermal expansion
FCT	furnace cycle test
HVOF	high-velocity oxyfuel spray
InCF	intrinsic chemical failure
MICF	mechanically induced chemical failure
PS	plasma spray
RE	reactive element
TBC	thermal barrier coating
TC	top coat
TCF	thermal cycling fatigue
TCP	topologically close-packed
TGO	thermally grown oxide
VPS	vacuum plasma spray
Y-PSZ	yttria partially stabilised zirconia

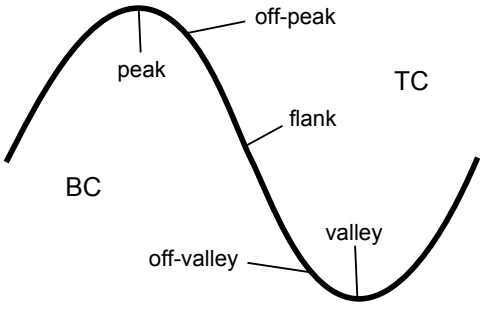

Bond coat/top coat interface.

Part I

Theory and background

1

Introduction

1.1 Background

Gas turbines are widely in use for power production and for aircraft propulsion, and the development of gas turbines towards higher efficiency and fuel economy is desirable. Such an increase in efficiency can be achieved by increasing combustion temperature, [1–5], and, consequently, the development of gas turbines over the last 50–60 years have driven the service temperature to higher and higher levels.

The desire to increase efficiency of gas turbines by increasing operating temperature offers several challenges in the field of engineering materials; as the operating temperature is driven to higher levels, material issues, (such as oxidation, corrosion, creep and microstructural degradation), are inevitable, [5–9]. The state-of-the-art materials for high temperature applications, the superalloys, are already operating at their maximum capacity and further increase in operating temperature can currently only be achieved by the use of thermal barrier coatings and air cooling, [4, 6, 8, 10–12]. Furthermore, the wish to build a more energy sustainable society, and to reduce environmental problems, has drawn attention to the use of bio-fuels in gas turbines, [13]. The incorporation of bio-fuels in gas turbine technology may inflict harsher operating conditions on metallic materials which will, again, lead to material issues.

The research presented in this thesis has been conducted as a part of the Swedish research programme TURBO POWER. The programme is run as a collaboration between Siemens Industrial Turbomachinery, Volvo Aero Corporation, the Swedish Energy Agency and several Swedish universities.

The research programme TURBO POWER seeks to:

- Improve fuel efficiency of power-producing turbomachines, thereby reducing emissions and decrease environmental degradation.
- Improve fuel flexibility by making possible the use of alternative fuels.
- Reduce operating costs of power-producing turbomachines.

By developing technology and knowledge for university and industry, TURBO POWER will contribute to a more sustainable and efficient energy system in Sweden. The research aims at being highly applicable for industry and governed by needs.

1.2 The role of coatings in achieving higher gas turbine efficiency

The basic structure of a gas turbine, as seen in fig. 1 a) and b), consists of three major parts: 1) the compressor, which compresses the air, 2) the combustor, in which air and fuel are mixed and ignited, and 3) the turbine which drives the compressor and provides the power output for electric power production. The later two, combustor and turbine, operate in a very demanding high-temperature environment and need to be protected to avoid degradation, [3, 5, 6, 10, 14–16]. Therefore, thermal barrier coatings (TBCs) are often used as an insulating and oxidation resistant barrier.

A simple motivation for the need of thermal barrier coatings is illustrated by fig. 2 which displays the variation of tensile strength with temperature for some common superalloys. As seen in fig. 2, superalloys cannot maintain their tensile strength at temperatures typical in gas turbine combustors. Furthermore, at high temperatures, phenomena such as creep, oxidation and corrosion occur rapidly and limit the life of metallic materials. To still enable high enough combustion temperatures in gas turbines, air cooling and thermal barrier coatings are commonly used, [1–4, 11, 15].

A schematic drawing of a thermal barrier coating system is shown in fig. 3 a), where the four parts of the thermal barrier system can be seen: 1) substrate, 2) bond coat (BC), 3) thermally grown oxides (TGOs), and 4) top coat (TC), [3]. The top coat consists of a ceramic layer which provides the necessary insulation, and the metallic bond coat ensures good adhesion of the ceramic coating and provides oxidation resistance, [9, 14]. Fig. 3 b) displays the insulating effect of TBCs; this insulating effect enables high combustion temperatures while avoiding high temperature degradation of metallic parts.

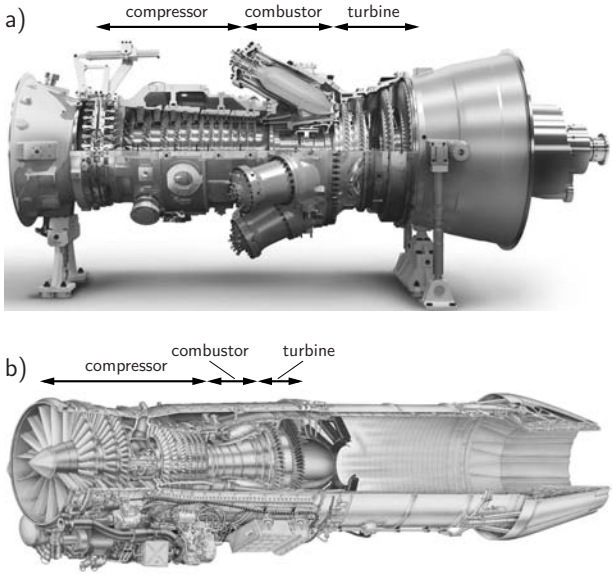

Figure 1: Gas turbines for power production and aircraft propulsion. a) Land-based gas turbine, SGT 750, for power production, (courtesy of Siemens Industrial Turbomachinery). b) Aircraft engine RM 12, used in JAS 39 Gripen, (courtesy of Volvo Aero Corporation).

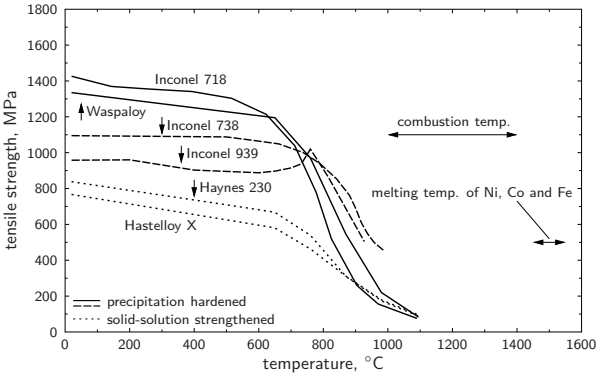

Figure 2: Tensile strength of some superalloys as function of temperature, (data from various superalloy manufacturers).

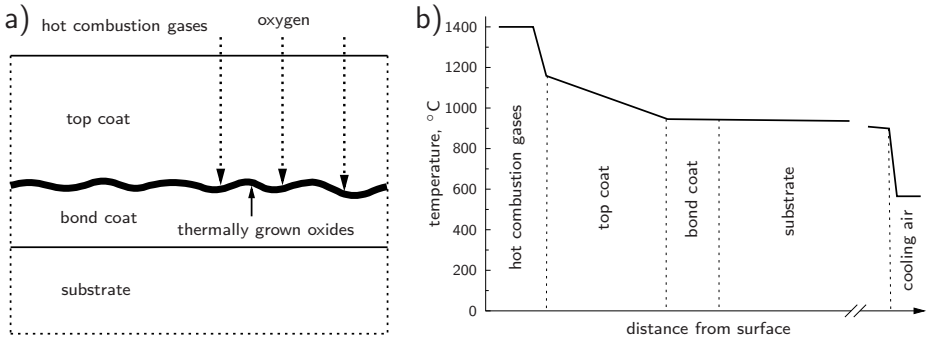

Figure 3: Thermal barrier coating system. a) A schematic drawing of a thermal barrier system: substrate, bond coat, thermally grown oxides and top coat. The thermally grown oxides are formed as oxygen penetrates the top coat and oxidises the bond coat. b) The benefits of thermal barriers illustrated by temperature variations through a coated component in a gas turbine, (based on ref. [1]).

As seen in fig. 2, the combustion temperature of gas turbines is already approaching the melting temperatures of the base-elements in superalloys, (nickel, cobalt and iron); the sought-after high combustion temperatures of tomorrow might very well exceed the melting temperature of the alloys used in structural elements in gas turbines, [3], which further stresses the importance of well-performing thermal barrier coatings and effective air cooling.

1.3 Purpose of research

Currently, thermal barrier coatings belong to the more effective solutions for increasing gas turbine combustion temperature and thereby increasing efficiency, [4, 6, 8, 10, 11]. To fully utilise the beneficial effects of protective coatings, the reliability of TBCs must be improved, [1, 11, 14]; the development of deeper understanding of TBC failure mechanisms and modelling of TBC life are therefore important areas of research, [1, 8, 9, 14].

There are a number of degrading mechanisms acting on TBCs that make TBCs susceptible to failure during service. The research presented in this thesis aims at adding to the current knowledge on degradation and failure of TBCs, which can be used as basis for life prediction of TBCs. The long-term aim of this research project is to extend and improve current TBC life models. As part of achieving this, the present work focuses on increasing knowledge of the degradation mechanisms leading to TBC failure and, hence, limiting TBC life.

2

Materials for high temperature applications

A high temperature material is a material that can operate at temperatures close to its melting temperature, while still maintaining many of the typical room temperature characteristics of engineering materials, such as high strength and microstructural stability. With the homologous temperature, T_{H}, defined as the operating temperature divided by the melting temperature (in Kelvin), $T_{\mathrm{H}} = T_{\mathrm{operating}}/T_{\mathrm{melting}}$, a material working at $T_{\mathrm{H}} \geqslant 0.6$ might be considered to work at high temperature, [8]. In addition, high temperature materials must resist degradation due to prolonged service at high temperature, such as: oxidation, corrosion and creep.

Three classes of alloys: Ni-base, Co-base and Fe–Ni-base, collectively referred to as superalloys, have shown to have good to excellent high temperature properties and are widely in use for high temperature applications, [6–8].

2.1 Physical metallurgy of Ni-base alloys

The solid solution γ-Ni phase, which has the FCC atomic arrangement, constitutes the matrix phase in Ni-base alloys. A number of alloying elements are added; the compositions of some common Ni-base alloys are given in table 1. Ni-base superalloys may be solid-solution strengthened, such as Haynes 230 and Hastelloy X, or precipitation hardened, such as Waspaloy and Inconel 738, 939 and 718. In the case of solid-solution strengthened alloys, alloying elements are typically chosen from: Co, Cr, Fe, Mo and W, either solved in the matrix or forming carbides, [6, 8].

Table 1: Composition of some Ni-base alloys

alloy	Ni	Co	Fe	Cr	W	Mo	Al	Ti	Nb	Ta	Si	C	B
Haynes 230	57[a]	5[b]	3[b]	22	14	2	0.3	–	–	–	0.4	0.1	0.015[b]
Hastelloy X	47[a]	1.5	18	22	0.6	9	–	–	–	–	1[b]	0.1	0.008[b]
Inconel 738	61.4[a]	8.5	–	16	2.6	1.75	3.4	3.4	0.9	1.75	–	0.17	0.01
Inconel 939	47.3[a]	19	0.5[b]	22.5	2	–	1.9	3.7	1	1.4	0.2[b]	0.15	0.01
Inconel 718	52.5	1[b]	18.4[a]	19	–	3.1	0.5	0.9	5.1	–	0.35[b]	0.08[b]	0.006[b]
Waspaloy	58[a]	13.5	2[b]	19	–	4.3	1.5	3	–	–	0.15[b]	0.08	0.006

[a] as balance
[b] maximum

For precipitation hardened alloys the alloying elements are typically chosen from: Al, Ti, Nb and Ta, which promotes the formation of the γ'-phase as precipitates in the γ-matrix, [6, 8], shown in fig. 4 a). The γ'-phase is an intermetallic phase with formula: $Ni_3(Al, Ti)$; the Al and Ti may be substituted by Nb, and the Ni can, to some extent, be substituted by Co or Fe. The γ'-phase is an ordered phase with the $L1_2$ superlattice structure. The γ'-phase may form precipitates of different morphology depending on their mismatch with the surrounding parent lattice; morphologies include: cubical, small spherical particles and arrays of cubes, [8]. Modern precipitation hardened alloys may contain $\gtrsim 60\,\%$ γ', [7, 8]. An interesting characteristic of γ' is its increasing tensile strength with increasing temperature.

While addition of Al and Ti promotes the formation of γ', addition of Nb might instead promote the formation of another precipitating phase: the $\gamma''-Ni_3Nb$, [6, 7]. The $\gamma''-Ni_3Nb$ forms in Fe–Ni-base alloys and may, for some alloys, be the primary strengthening microconstituent, such as in Inconel 718. Alloys that rely on the strengthening of $\gamma''-Ni_3Nb$ are limited to operating temperatures below $\sim 650\,°C$ as the tetragonal $\gamma''-Ni_3Nb$ otherwise will transform to a stable orthorhombic $\delta-Ni_3Nb$ which does not add to strength, [7].

The addition of C and B enables the formation of carbides and borides. Carbide formers include Cr, Mo, W, Nb, Ti, Ta and Hf, which form carbides of various stoichiometry, such as MC, $M_{23}C_6$ and M_6C. Common boride formers are: Cr and Mo, which form M_3B_2; boron tends to segregate to grain boundaries, [6, 7].

The MC carbide forms at high temperatures, (typically during solidification and cooling in the manufacturing process), while $M_{23}C_6$ and M_6C form at lower temperatures 750–1000 °C, [6]. The MC carbide typically forms from Ti, Hf and Ta, but substitution might occur so carbides of the form (Ti, Nb)C, (Ti, Mo)C and (Ti, W)C are common, [7, 8]. The $M_{23}C_6$ is promoted by high Cr contents and the M_6C is promoted by large fractions of W and Mo, [6]. While the MC carbide may be formed within grains as well as at grain boundaries, the $M_{23}C_6$ carbides are preferably formed at grain boundaries.

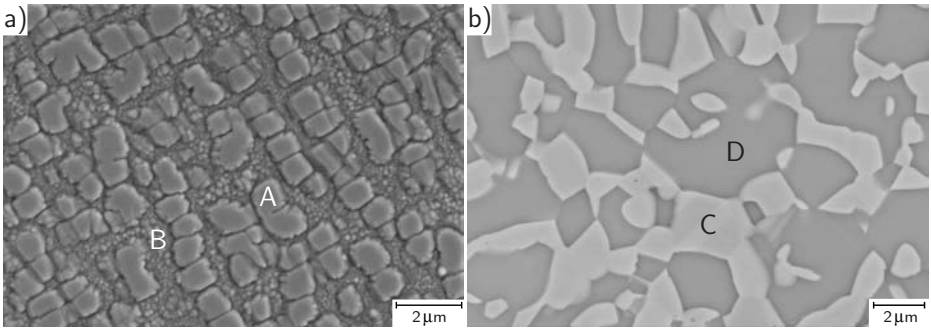

Figure 4: Some microconstituents in Ni-base alloys. a) Secondary electron image of Ni-base superalloy Inconel 792 showing: A γ' precipitates, B γ-matrix with secondary γ'. b) Backscatter electron image of an aluminium rich Ni-base alloy of NiCoCrAlY type. C denotes γ or γ/γ' and D denotes β.

Since MC carbides form already during manufacturing, they constitute the main source of carbon in the alloy. During high temperature exposure, due to service or heat treatment, the MC carbides may decompose to form carbides of the $M_{23}C_6$ and M_6C type. The following reactions have been suggested, [6]:

$$MC + \gamma \longrightarrow M_{23}C_6 + \gamma' \tag{A}$$

and

$$MC + \gamma \longrightarrow M_6C + \gamma' \tag{B}$$

A group of intermetallics generally considered harmful to Ni-base alloys, are the topologically close-packed (TCP) phases; these phases may precipitate in alloys rich in Cr, Mo and W, [8]. Several phases of varying crystal structure and stoichiometry exist, but only one is mentioned here: the σ-phase. This phase has the general formula $(Cr, Mo)_x(Ni, Co)_y$, [6]; it may have a plate or needle-like morphology and may appear in grain boundaries, sometimes nucleated from grain boundary carbides, [6, 7].

2.2 Thermal barrier coating systems

A protective coating for high temperature applications must provide, [10]:

- Low thermal conductivity.
- Good oxidation and corrosion resistance.

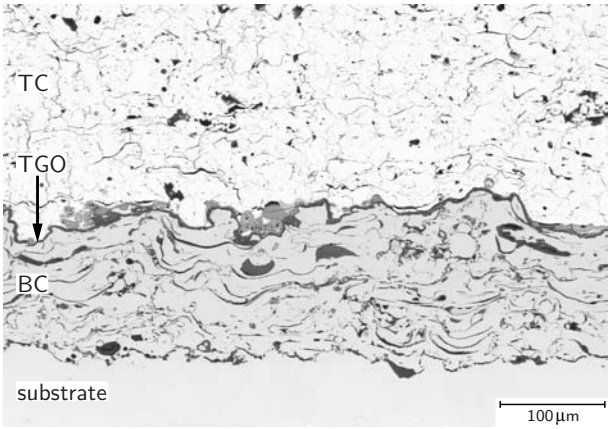

Figure 5: The components in a thermal barrier system: substrate, bond coat (BC), thermally grown oxides (TGO) and top coat (TC).

- High melting temperature and no detrimental phase transformations in the operating temperature interval.

- A coefficient of thermal expansion (CTE) as close as possible to the substrate on which it is deposited.

As no single material possesses all of those properties, protection of superalloys is typically achieved by material systems, (thermal barrier coating systems), comprising an insulating layer, (the top coat), and an oxidation resistant layer, (the bond coat). A TBC system is shown in fig. 5.

2.2.1 Top coat materials

The top coat is the part of the TBC system that provides insulation, and thus protects the underlying substrate from high temperature. The top coat introduces a temperature gradient, (as illustrated in fig. 3 b)), and must be combined with internal cooling of the substrate. Provided the cooling is sufficient, the temperature drop in a top coat, 300 µm in thickness, can be as high as 200–250 °C, [3, 7, 8, 10]. The 6–8 wt.% yttria partially-stabilised–zirconia (Y-PSZ) has become the standard material for thermal barriers, [17]. This is due to the combination of its low thermal conductivity and relatively high coefficient of thermal expansion, [3, 17].

Pure zirconia (ZrO_2) is allotropic with three possible crystal structures: monoclinic up to 1170 °C, tetragonal in the interval 1170–2370 °C and cubic

up to the melting point at 2690 °C. The tetragonal–monoclinic transformation is especially problematic since it occurs at a temperature in the range of the service temperature in gas turbines. The tetragonal $\longrightarrow$ monoclinic transformation is martensitic in nature and involves a 3–5 % volume increase that induces internal stresses which compromises the structural integrity of the ceramic, [10, 18].

This can be solved by adding 6-8 wt.% of yttria (Y_2O_3) to the zirconia lattice, which stabilises a *non-transformable tetragonal* phase, t′, which is stable from room temperature to approximately 1200 °C, [3, 8, 17]. Other stabilising oxides can also be used, such as MgO, CaO, CeO_2, Sc_2O_3 and In_2O_3, [10, 12, 17]. The t′ phase is formed by rapid cooling during coating deposition and is a metastable phase, [17]. At high temperature exposure this metastable phase starts to transform to the equilibrium tetragonal and cubic phases, thereby enabling the undesired tetragonal $\longrightarrow$ monoclinic transformation on cooling, [19].

The t′ $\longrightarrow$ cubic + tetragonal transformation occurs as the Y-PSZ is only partially stabilised. The addition of $\gtrsim 11$ wt.% of Y_2O_3 would stabilise the cubic phase from room temperature to melting temperature and thus enabling higher operating temperatures. The choice of 6–8 wt.% yttria relies on empirical investigations made by Stecura, [20], who found that 6–8 wt.% of yttria gave the longest fatigue life during thermal cycling.

2.2.2 Bond coat materials and thermally grown oxides

While the Y-PSZ top coat provides the necessary thermal insulation, it does not offer any protection against oxidation and corrosion. The Y-PSZ readily lets oxygen through and causes the underlying metal to oxidise, [17]. This is avoided by the incorporation of an oxidation resistant bond coat between the substrate and the top coat. Furthermore, the bond coat improves adhesion between the top coat and the substrate. Bond coats typically consist of MCrAlX where M constitutes the base of the alloy and is Ni, Co or Fe, (or a combination), and X symbolises minor amounts of reactive elements (REs), most commonly $\lesssim 1$ wt.% Y, [3, 5, 9, 14, 17, 21, 22].

Al and Cr are added in amounts of > 5 wt.% to improve oxidation and corrosion resistance by formation of a protective scale of thermally grown oxides (TGOs) in the BC/TC interface. MCrAlY coatings rely on the formation of such protective oxide scales for oxidation and corrosion resistance. Such a protective scale needs to be: stable at high temperatures, dense, slow-growing and exhibit good adhesion to the coating, [12]. Three oxides have the potential to fulfil these requirements: alumina (Al_2O_3), chromia (Cr_2O_3) and and silica (SiO_2), [12, 23]. At such high temperatures as are common

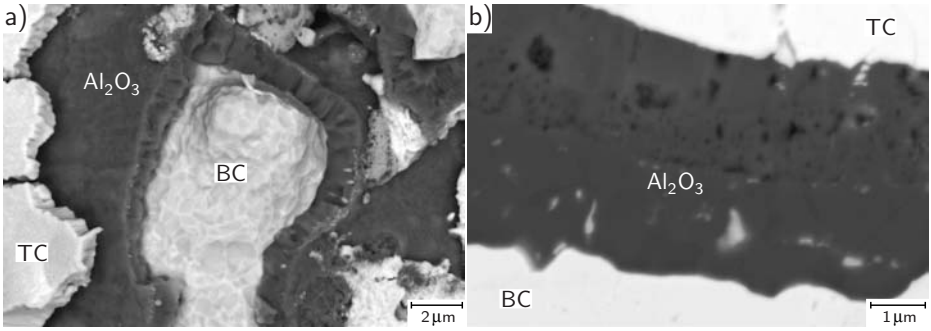

Figure 6: Protective layers of thermally grown Al_2O_3 in the BC/TC interface. a) A torn off top coat has revealed the interfacial TGO and part of the bond coat. b) A cross-section showing a protective layer of Al_2O_3.

in gas turbines, a continuous layer of alumina is considered to be the most beneficial for TBC life, [7, 9]. The use of Cr_2O_3-forming coatings is usually restricted to somewhat lower temperatures, ($\lesssim 950\,^{\circ}\mathrm{C}$, [7, 12]), as Cr_2O_3 may decompose to volatile CrO_3 and evaporate, thus breaking the protective scale. However, the addition of Cr promotes the formation of a protective Al_2O_3 scale, [12]. The use of SiO_2-forming coatings is also limited to lower temperature as it may form low-melting or brittle phases; Si diffuses readily into the substrate and large amounts might be necessary to form protective scales, [12]. A protective layer of Al_2O_3-rich interface TGOs can be seen in fig. 6 a) and b): fig. 6 a) shows a fracture surface produced by tearing off the top coat, thus exposing the underlying interface TGO and fig. 6 b) shows a polished cross-section of a layer of interfacial TGO.

The interfacial TGO is protective only as long as it consists of predominantly Al_2O_3, and as long as it is intact and adherent to the bond coat. The composition of the bond coat must therefore be chosen to account for the depletion of aluminium during high temperature exposure by consumption of Al through oxidation and interdiffusion of Al with a low-aluminium substrate; most bond coats are, consequently, quite rich in Al, [17]. To improve scale adhesion REs are added; even RE additions in the order of $\sim 0.1\,\mathrm{wt.\%}$ may increases adhesion of the Al oxide scale, [24].

The Ni–(0–30 wt.%Co)–(10–30 wt.%Cr)–(5–20 wt.%Al)–($\lesssim 1\,\mathrm{wt.\%Y}$) alloy covers the range of many bond coat compositions. Being a Ni-base alloy, it consists of a γ-matrix with some of the aluminium possibly bound in the γ' aluminide. However, for such large amounts of Al as are commonly used in NiCoCrAlY, yet another aluminide forms: β-NiAl, [12, 25]; most of the aluminium is bound in this phase, and the two main microconstituents of

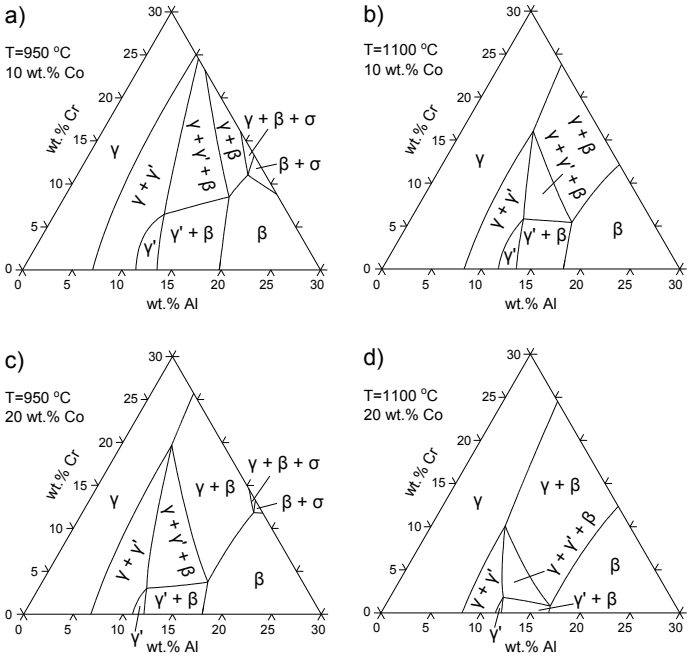

Figure 7: Phase diagrams for some NiCoCrAl alloys established by THERMO-CALC calculations. a) NiCrAl + 10 wt.% Co at 950 °C b) NiCrAl + 10 wt.% Co at 1100 °C c) NiCrAl + 20 wt.% Co at 950 °C d) NiCrAl + 20 wt.% Co at 1100 °C

NiCoCrAlY is γ and β, shown in fig. 4 b). In addition, NiCoCrAlY may contain the TCP phase $\sigma{-}(\mathrm{Cr}, \mathrm{Co})$ and solid solution α-Cr, [25]. The latter may occasionally precipitate in the β-phase, [25, 26]. Thus, a typical NiCoCrAlY alloy may have microstructures such as: $\gamma + \beta$ or $\gamma/\gamma' + \beta/\alpha$ both with the occasionally addition of $\sigma{-}(\mathrm{Cr}, \mathrm{Co})$, [27–29]. Fig. 7 shows the phases present at high temperature for the Ni–Cr–Al system with different additions of Co.

As the NiCoCrAlY forms Al-rich TGOs and, consequently, the Al content in the coating drops, β will dissolve, thereby freeing Al for further oxidation. Depending on oxidising temperature and fraction of Co and Cr, the stable phases, (not considering α and σ), can be either $\gamma + \beta$ or $\gamma + \gamma' + \beta$. Depending on whether γ' is stable or not, two possible decomposition routes are, [7, 12, 30]:

$$\beta \longrightarrow \gamma \tag{C}$$

and

$$\beta \longrightarrow \gamma + \gamma' \longrightarrow \gamma \tag{D}$$

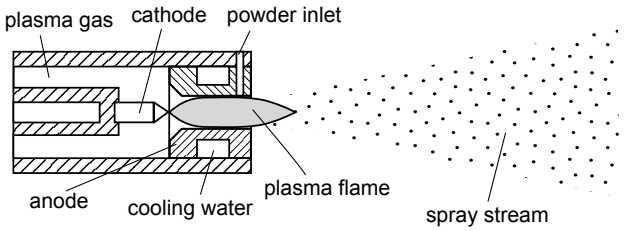

Figure 8: Schematic drawing of a plasma gun, (based on ref. [31]).

2.3 Manufacturing of TBCs

The group of manufacturing methods referred to as *thermal spraying* include processes such as plasma spraying (PS) and high-velocity oxyfuel spraying (HVOF), both commonly in use for manufacturing of TBC systems, [16, 17]. As all TBC systems used in the current research project are plasma sprayed, that is the only manufacturing method that will be explained here.

The raw material for manufacturing of bond coats and top coats are typically in powder form. The plasma spray process uses a plasma jet to melt the feedstock powder and propel it towards the substrate. Feedstock powder is introduced by a carrier gas into the plasma jet, melted and propelled towards the substrate, [16]. A schematic drawing of a plasma gun is displayed in fig. 8. The plasma gas, usually an inert one such as argon, is brought into the plasma gun and led through an electric field that ionises the gas and produces plasma; the plasma may reach temperatures as high as 20 000 °C, [16]. Due to the high temperature, the anode is water cooled and the cathode is typically made from tungsten which has a sufficiently high melting temperature (and is a good thermionic emitter), [16]. Plasma spraying can be conducted in air or in vacuum and is, accordingly, referred to as air plasma spraying (APS) and vacuum plasma spraying (VPS).

2.3.1 Microstructure in thermal spray coatings

The plasma spraying process gives rise to a very characteristic microstructure. As the molten droplets impact on the substrate they form thin disk-shaped lamellae, or splats, which cool on impact and solidify rapidly, (in the case of metal coatings: with a speed of up to 10^6 K/s, [16]). Such high cooling rates might cause metastable phases to form and typically promote the formation of a very fine grain structure or even amorphous phases.

In the case of metallic coatings, the microstructure of an air plasma sprayed coating includes constituents such as: splats, oxide inclusions/string-

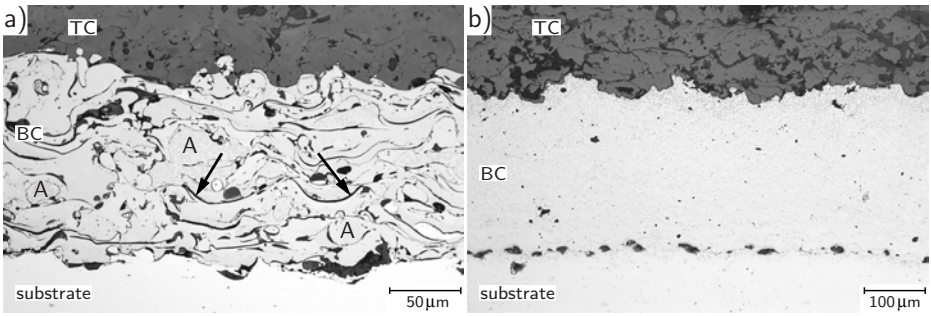

Figure 9: Microstructure in two plasma sprayed MCrAlY coatings, light–optic microscopy. a) Air plasma sprayed coating where the oxide inclusions/stringers are clearly visible, marked by arrows. Also visible are the unmelted, or partially melted, particles, marked by A. b) Vacuum plasma sprayed MCrAlY without oxide stringers and with lower porosity.

ers, pores and unmelted or partially melted particles. The microstructural characteristics of an APS deposited bond coat are shown in fig. 9 a) and can be contrasted to a VPS deposited bond coat, shown in fig. 9 b), whose characteristic features are the absence of oxide stringers and lower porosity.

In the case of ceramic coatings, the rapid solidification typically causes a columnar grain structure within each splat, shown in fig. 10 a), [32, 33]. The splat–on–splat structure, typical of plasma spraying, is seen in fig. 10 b) where it can also be seen that the splats segment by forming a cracked–mud-like pattern of intralamellar microcracks. Such cracking is due to internal stresses imposed by the contraction on cooling of the splat while being partially restricted by the underlying layer of splats, [32]. Fig. 10 b) also shows another type of crack-like defects caused by the plasma spraying: interlamellar delaminations, [17, 32, 34–36]. The area of contact between layer of splats may be as low as 20 %, [37], and it is these crack-like voids between splats that constitute the interlamellar delaminations. Both the intralamellar microcracks and interlamellar delaminations can be readily seen on cross-sections, as shown in fig. 10 c). Furthermore, APS gives rise to porosity, and in the case of the top coat such porosity is desirable as it decreases the thermal conductivity of the coating, [17]; porosity levels in TBCs typically lies in the interval 5–20 %, fig. 10 d).

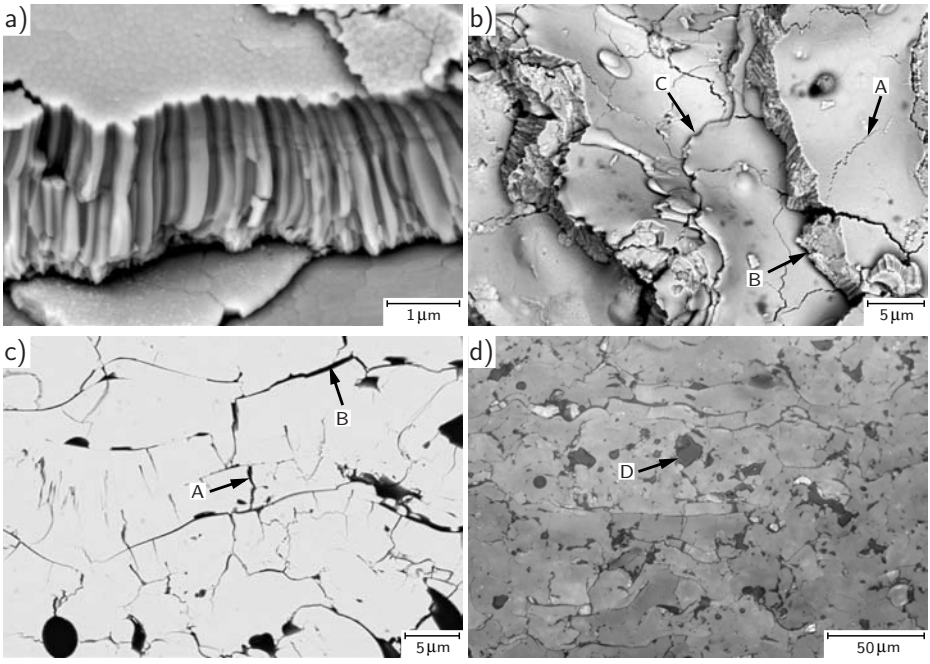

Figure 10: Microstructural characteristics of an air plasma sprayed Y-PSZ top coat. a) Backscatter electron image showing the typical columnar grain structure in a rapidly solidified splat. b) A fractured top coat showing the typical splat–on–splat structure, C, and, consequently, the interlamellar delaminations, B. Also visible is the internal cracking of the individual splats, A. Backscatter electron image. c) Cross-section of a top coat showing interlamellar delaminations, B, and through-splat cracks, A. Backscatter electron image. d) Light-optic image of a cross-sectioned top coat, displaying the porosity, D.

3

High temperature degradation of coatings

3.1 Oxidation

While the formation of a protective layer of BC/TC interface TGOs is essential for oxidation resistance of TBC systems, the oxidation is at the same time a degrading mechanism that will eventually lead to the breakdown of the protective TGO and might induce failure of TBCs. The oxidation of the BC can be divided in three stages, shown in fig. 11: 1) a *transient stage* of simultaneous oxidation of all oxide-forming species in the BC, 2) a *steady-state stage* of formation and growth of a protective oxide scale, and 3) a *breakaway stage* of rapid oxidation and spallation, [23].

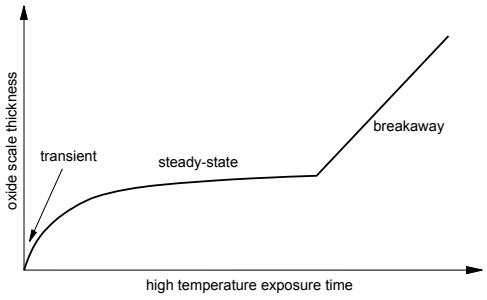

Figure 11: Schematic drawing of the three stages of oxidation: short stage of transient oxidation followed by steady-state oxidation and, finally, an increase in oxidation rate that marks the start of the breakaway oxidation, [23].

3.1.1 Build-up and maintenance of a protective oxide layer

The transient stage is the stage of oxidation before a continuous oxide layer has formed on the metal surface and during which all oxide-forming species in the alloy, (Ni, Co, Cr, Al, etc.), might form oxides. The transient stage is usually quite short, typically $\lesssim 1\,\mathrm{h}$ for Ni–Cr–Al systems oxidised at 1000–1200 °C, [38, 39]. The composition of the transient oxides is influenced by parameters such as: temperature, partial oxygen pressure, coating composition and coating microstructure, [40]; low partial oxygen pressure, for example, may decrease the amounts of transient non-aluminium oxides. Transient oxides include Cr_2O_3, NiO, CoO, spinel type $(Ni, Co)(Cr, Al)_2O_4$ and various forms of alumina: γ-, θ-, α-Al_2O_3, [30, 38–42].

Following the transient stage comes the steady-state stage during which one oxidising species becomes dominant and forms a continuous layer on the metal surface; as soon as the continuous layer is formed oxidation rate becomes controlled by the diffusion rate of oxygen and metal ions through the oxide layer. Such diffusion controlled oxidation is typically described by a power-law expression.

$$h_{\mathrm{TGO}} = h_0 + kt^{\frac{1}{n}}, \quad \text{n=2–3} \tag{1}$$

where h_{TGO} is the thickness, (or weight gain per oxidised area), of the formed oxide, h_0 is the thickness of the transient oxides, k is a constant and t is the high temperature exposure time. The classical oxidation law is parabolic ($n = 2$), [43], but subparabolic models ($1/n < 0.5$) are also in use, [9, 44–46].

Oxides that slow down oxidation, (by lowering the diffusion rate through the oxide), are protective. Protective oxide scales can be provided by Al, Cr and Si which forms Al_2O_3, Cr_2O_3 and SiO_2, [7, 9, 23]. At high temperature, Al_2O_3 is usually the protective coating as Cr_2O_3 may decompose to CrO_3 for temperatures higher than 1000 °C according to the reaction, [7, 9, 47]:

$$Cr_2O_3(\mathrm{solid}) + \tfrac{3}{2}O_2(\mathrm{gas}) \rightleftharpoons 2\,CrO_3(\mathrm{gas}) \tag{E}$$

The oxidation can be either internal or external as explained in fig. 12; in order for the oxide layer to be protective it must be external. For a given alloy composition, there exists a minimum concentration of aluminium for which a external protective oxide layer can form. In a Ni–Al system with low fraction of Al, internal oxidation will occur if the diffusion of Al to the metal/air boundary is slower than the diffusion of oxygen into the alloy; in such alloys the Al will not be able to reach the metal/air boundary as it will oxidise internally due to the high concentration of oxygen in the alloy. The depth,

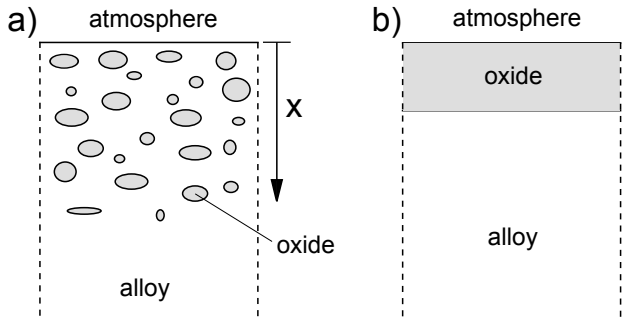

Figure 12: Two types of oxidation: a) Internal oxidation where the concentration of the oxidising element is low and the inward diffusion of oxygen is high, causing the oxidising element to form a subscale of oxide precipitates to depth x. b) External oxidation where the oxidising element forms a protective oxide layer.

x, of the internally oxidised layer, or subscale, at time t is approximately, [7]:

$$x = \left(\frac{2N_O D_O t}{\nu N_M}\right)^{\frac{1}{2}} \tag{2}$$

where N_O is the mole fraction of oxygen in the metal close to the surface, D_O is the diffusivity of oxygen in the alloy, ν is the ratio of oxygen to metal atoms of the formed oxide and N_M is the mole fraction of the oxide forming element, (Al in the Ni–Al system). It is evident from equation 2 that the subscale thickness decreases as mole fraction Al increases, eventually a shift to external oxidation occurs. For Ni–Al alloys with high enough fraction of Al, Al will be readily available to form oxides at the metal/air boundary and an external oxide layer will form. In binary alloy systems, such as Ni–Al, the amount of Al needed to cause a shift from internal to external oxidation is $\gtrsim 17$ wt.%, [6].

The addition of chromium will lower the fraction of Al needed to form an external oxide layer by acting as a *getter* for oxygen, [48]. As seen from equation 2, the internal oxidation can be decreased by lowering the mole fraction of oxygen in the metal close to the surface, (thereby lowering the amount of oxygen diffusing into the alloy). This can be achieved by the addition of another reactive element, such as Cr, that getters, (retains), oxygen by forming chromia.

An estimate of what kind of oxides will form can be obtained by an *oxide map*, such as the one showed in fig. 13 for the Ni–Cr–Al system. For example, fig. 13 shows that ~ 20 wt.% Al, (~ 35 at.% Al), is needed to ensure Al_2O_3 growth in a Ni–Al system, but with the addition of 5 wt.% Cr, (~ 5 at.%), the alloy can form Al_2O_3 at an Al content as low as ~ 5 wt.%, (~ 10 at.%).

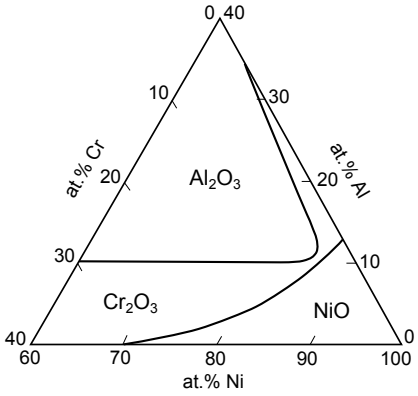

Figure 13: Oxide map for the Ni–Cr–Al system at 1000 °C, (based on ref. [49]). Areas denoted Cr_2O_3 and NiO might also give internal oxidation of Al_2O_3.

Although steady-state oxidation is governed by the growth of a continuous layer of protective Al_2O_3, minor amounts of oxides of deviating composition may form in the BC/TC interface even during the steady-state stage, [50]. Such oxides may form either as a chromium rich layer between the Al_2O_3 and TC or as bulky clusters containing a mixture of several types of oxides, such as: $(Al, Cr)_2O_3$ (chromia), $Ni(Al, Cr)_2O_4$ (spinels) and NiO, [50]. Such clusters of chromia–spinel–nickel oxide may form quite early during oxidation, and form in greater quantities with higher temperature, but remain fairly constant during the steady state stage, [50].

A common bond coat typically has the generic formula MCrAlX, where X is chosen from the group of reactive elements (RE), such as Y, Hf, Zr, Ce or La, [10, 17, 21]. REs are generally considered to improve the oxide scale adhesion; several mechanisms have been suggested:

- REs tie up sulphur which would otherwise have segregated to the metal/oxide interface and lowered the metal/oxide adhesion, [17].

- REs may alter the oxide growth mechanism from an outward growing to an inward growing oxide scale, [24].

- REs may form oxides in the metal/oxide interface and mechanically pin the oxide to the metal by so called *pegging*.

The most common RE is Y. The Y readily forms oxides and may be found in the Al_2O_3 scale as: yttria Y_2O_3, yttrium aluminium perovskite (YAP) $YAlO_3$ and yttrium aluminium garnet (YAG) $Y_3Al_5O_{12}$, [40].

3.1.2 Breakdown of the protective oxide layer

During prolonged exposure to high temperature, aluminium depletion will occur in the bond coat as aluminium is consumed by oxidation and interdiffusion with a low-aluminium substrate, [9, 22, 45]. The interfacial TGO will remain protective only as long as the BC contains enough Al to maintain a continuous layer of Al_2O_3. An aluminium concentration of $\geqslant$3–5 wt.% is generally enough to maintain the Al_2O_3 layer, [6, 7, 51, 52], but for a lower Al content non-protective oxides will start to form in the BC/TC interface and the oxidation rate increases; this marks the onset of breakaway oxidation, or *chemical failure*.

The chemical failure can be divided into two groups: mechanically induced chemical failure (MICF) and intrinsic chemical failure (InCF), [53]. MICF occurs if the protective oxide layer cracks and the Al content is to low to heal the protective layer. InCF occurs when the Al content beneath the oxide layer drops to such a low level that the Al_2O_3 is no longer the preferred oxide. This condition results in the formation of other oxides, either from the alloy or by decomposition of the alumina scale according to reactions such as, [45]:

$$Al_2O_3 + 2\,Cr \longrightarrow Cr_2O_3 + 2\,Al \tag{F}$$

or

$$Al_2O_3 + \tfrac{1}{2}O_2 + Ni \longrightarrow NiAl_2O_4 \tag{G}$$

The Al_2O_3 is eventually replaced, (or partially replaced), by a layer of chromia $(Cr, Al)_2O_3$, spinel $(Ni, Co)(Cr, Al)_2O_4$, nickel oxide and cobalt oxide, [30, 39, 54–57]; the now non-protective interface TGOs may also cause extensive internal oxidation of remaining aluminium, [55]. The layer of chromia and spinels has lower interfacial fracture resistance and once breakaway oxidation has started, the top coat might very well spall on cooling, [9, 30, 53, 55].

3.2 Fatigue

Not considering applied mechanical load, there are two sources for stresses in the TBC system: 1) interfacial TGO growth stresses and 2) mismatch stresses that develop on heating or cooling due to the differences in coefficient of thermal expansion between the bond coat, interface TGO and top coat, [17]. Both sources of stress act in the interface and failure of TBC systems consequently occurs by fracture in, or close to, the BC/TC interface, [9].

As the TBC system is exposed to thermal cycling, (i.e. gas turbine starts and stops during service), the mismatch in CTE will cause cyclic stresses and make the TBC system susceptible to fatigue. The thermal mismatch stresses are often considered to be most severe during cooling, since during heating, stress relaxation may occur; during cooling, however, there is no time for stress relaxation and stresses develop in the BC/TC interface that depend on the temperature drop, (larger temperature drop gives higher stresses), [56, 58]. For large temperature drops, (typical in gas turbines), the thermal mismatch stresses during cooling by far dominate over the TGO growth stresses, [17].

It should be noted that the thermal mismatch stresses depend not only on the temperature drop and the mismatch in CTE, but also on BC/TC interface morphology and the thickness of the interface TGOs, [59]. While the interface morphology is rather the same throughout the life of the TBC system, the TGO thickness and composition changes during the service life of the TBC system and thus changes the BC/TC interface stress distribution.

Based on finite element modelling, [60], the following simplified description of the BC/TC interface stress distribution would give at least a rough idea of the developed stresses: As the TBC system is heated to service temperature, stresses are introduced in the BC/TC interface due to a difference in CTE between BC and TC; however, at high temperature stress relaxation occurs rapidly and the TBC system will become essentially stress free after long enough high temperature exposure times. During high temperature exposure, interface TGO growth stresses will develop; however, they too might relax to some extent, or even completely. At cooling, on the other hand, there is no time for stress relaxation and stresses are introduced due to differences in the CTE. In a sinusoidal BC/TC interface, this will cause tensile stresses perpendicular to the interface to form at the interface peaks and compressive stresses perpendicular to the interface at interface valleys, as shown in fig. 14 a). As the interface TGOs thicken, the stress distribution will be affected, as shown in fig. 14 b) and c). A thicker TGO will cause the compressive stresses at the valleys to shift to tensile stresses. Such a stress distribution will be able to propagate a fatigue crack in the vicinity of the BC/TC interface, and, consequently, thermally cycled TBCs typically fail by fatigue.

3.2.1 Crack nucleation mechanisms

The typical splat–on–splat structure in plasma sprayed top coats combined with the rather modest degree of inter-splat adhesion, ($\sim 20\,\%$ contact area), give rise to many crack-like defects in the top coat. These pre-existing inter-

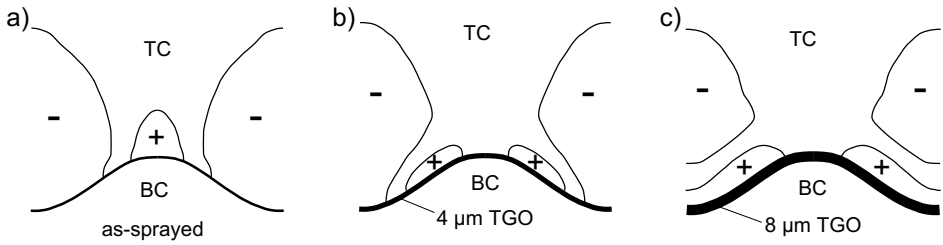

Figure 14: Out–of–plane (vertical) stresses in the TC close to the BC/TC interface. The compressive stresses at the valleys can be seen to shift to tensile stresses as the TGO grow, (based on ref. [60])

lamellar delaminations in the top coat, (see section 2.3.1), may act as crack embryos. Several papers have attributed crack nucleation to the opening of such interlamellar delaminations, [54, 61–66].

In addition to the pre-existing interlamellar delaminations in the top coat, cracks may also nucleate in the interfacial TGO during cycling. There are a few such crack initiation mechanisms described in literature; crack initiation in the BC/TC interface is most commonly attributed to peak and off-peak positions in the BC/TC interface. During cycling, the layer of interfacial Al_2O_3 may delaminate at peak positions thus thinning the protective TGO, or even completely exposing the metallic bond coat to oxygen. The TGO will reform and continue to grow beneath the unattached layer; after reaching sufficient thickness, the newly formed TGO may again delaminate and the process is repeated. Such repeated delamination and regrowth will give rise to a layered TGO structure at peak position which may act as starting points for larger delamination cracks, [21, 67–69], shown in fig. 15 a). Even without this delamination–regrowth-mechanism, cracks have been reported to be able to initiate at peak positions in the TGO, [67, 70, 71]. Another starting point for cracks in the TGO may be the voluminous clusters of chromia and spinels that may form rather early during high temperature exposure, (see section 3.1.1), [50, 54, 65, 66], shown in fig. 15 b).

3.2.2 Crack growth mechanisms

Many of the suggested crack growth mechanisms have in common that they focus on what happens in a *unit cell* of the BC/TC interface, typically a peak and a valley of a sinusoidal BC/TC interface. It is then assumed that crack growth as the one in the unit cell also occurs simultaneously throughout the BC/TC interface, and that failure occur by coalescence of such microcracks, forming larger cracks witch causes the top coat to buckle and spall off, [9].

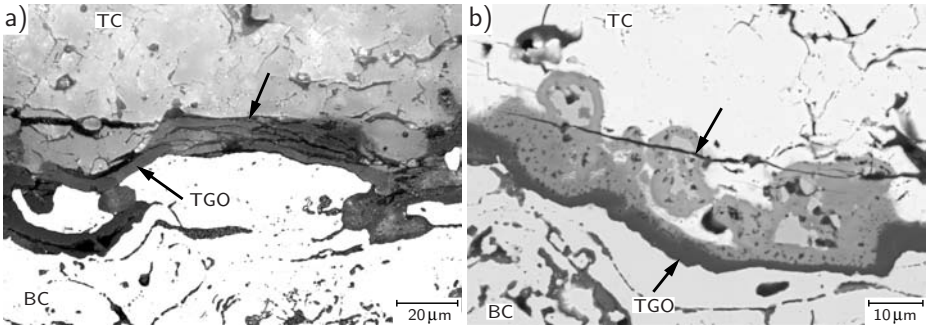

Figure 15: Crack formation in the interfacial TGO. a) Repeated cracking and regrowth giving a layered structure in the TGO. b) Cracking in a cluster of chromia, spinels and nickel oxide.

A few crack growth mechanisms from the literature will be described here. The one shown schematically in fig. 16 assumes crack initiation at asperities in a sinusoidal BC/TC interface, fig. 16 a). The ensuing crack growth will then either follow the BC/TC interface, fig. 16 b), or kink out in the TC, fig. 16 c). Such crack growth is assumed to occur at every peak in the BC/TC interface and failure occurs when such microcracks meet and coalesce.

The mechanism shown in fig. 17 occurs by the opening and slow growth of the pre-existing interlamellar delaminations in the top coat. Such microcracks grow in the vicinity of BC/TC interface peaks and eventually encounter a BC peak and arrest, fig. 17 a). Meanwhile, the thickening of the interface TGO will increase the out-of-plane tensile stresses at off-peak positions, and when such stresses are high enough, the cooling of the TBC system will cause the arrested TC microcracks to nucleate cracks in the TGO at peak positions, fig. 17 b). The crack propagation then proceeds until several of these cracks coalescence and cause failure, fig. 17 c), [61, 62].

Another mechanism suggests that cracks initiate from pre-existing delaminations in the top coat, just above the bond coat peak positions, fig. 18 a). Such cracks initiate early, while the out-of-plane stresses are tensile at peak positions but still compressive at valley positions, as shown in fig. 14 a). Since the cracks cannot grow through the areas of compressive stresses at flank and valley positions, the crack arrests until the thickening of the TGO changes the flank and valley stresses into tensile stresses as shown in fig. 14 b) and c). Crack growth occurs in the top coat and the failure occurs as these cracks coalesce, fig. 18 b), [63, 64].

In addition to internal crack growth, cracks may also grow from the edges of the TBC coated specimens, [72, 73]. Edge cracking occurs due to the

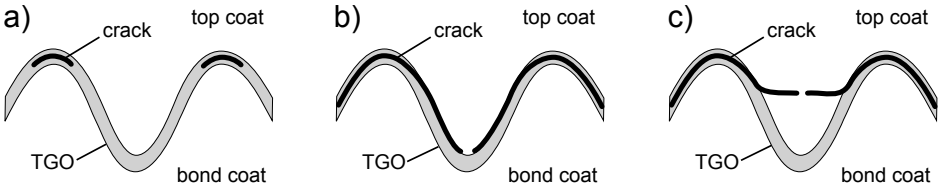

Figure 16: Crack nucleation in TGO, a), followed by either b) crack growth in, or close to the TGO or c) crack growth by kinking out in the TC.

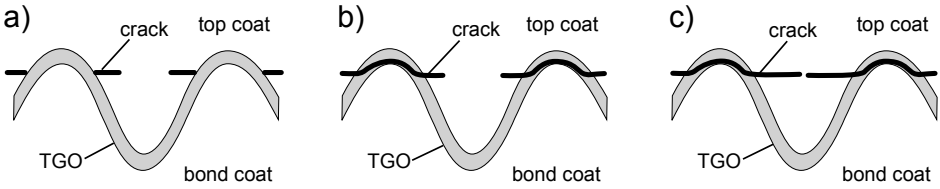

Figure 17: Crack nucleation in the top coat, a), followed by b) damage of TGO and c) crack growth.

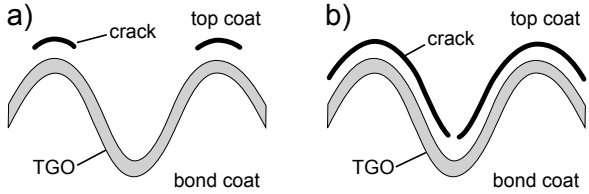

Figure 18: Crack growth in the top coat: a) nucleation and b) growth.

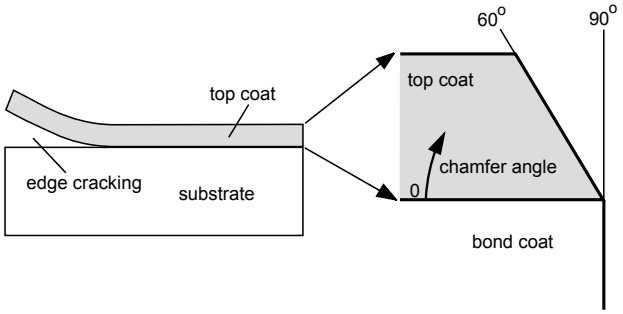

Figure 19: Edge cracking in TBCs.

stress concentration at TBC edges. Sjöström and Brodin, [72], investigated the influence of the chamfer angle on the risk of edge cracking in TBCs and found that any chamfer angle larger than 60 ° gave essentially the same risk whereas an angle of < 60 ° gives a lower risk of edge cracking, fig. 19.

Fracture that occurs in the TC is called *white fracture* and fracture that occurs in the BC/TC interface is called *black fracture* as the fracture surfaces will appear white and black respectively. Cracks that grow partly in the BC/TC interface and partly in TC is referred to as *mixed fracture*.

3.2.3 Fatigue life assessments

A few of the available TBC spallation life models will be briefly described here. The models that rely on finite element modelling only model a unit cell of the BC/TC interface, (as explained in section 3.2.2); cracks are assumed to initiate at the peaks in the BC/TC interface and then propagate in, or close to, the BC/TC interface and are thus controlled by the stress distribution in the BC/TC interface. Since such crack propagation is assumed to occur simultaneously all over the BC/TC interface, the fracture criterion can be set to failure when the microcracks reach the valleys, as they are then assumed to coalesce and cause spallation, as shown in fig. 16, 17 and 18.

Aluminium depletion models

Due to the strong dependence of TBC life on TGO growth, a possible approach to a life assessment would be to model the aluminium depletion from the bond coat. As the aluminium content reaches a critical value, the protective interface oxide layer can no longer be maintained and chemical failure commences. By modelling oxidation kinetics and, optionally, also interdiffusion, working TBC life models have been established, [51, 74–76].

The NASA model

The NASA model, [77], takes its starting point in a Coffin–Manson type expression

$$N = \left(\frac{\Delta\varepsilon_i}{\Delta\varepsilon_f}\right)^b \tag{3}$$

where N is cycles to failure, $\Delta\varepsilon_i$ is the inelastic strain range, $\Delta\varepsilon_f$ is the inelastic strain range that causes failure in one cycle and b is a constant. The effect of high temperature exposure on life is included via $\Delta\varepsilon_f$. The NASA model assumes the thickening of the TGO to influence life through the expression:

$$\Delta\varepsilon_f = \Delta\varepsilon_{f0}\left(1 - \frac{\delta}{\delta_c}\right)^c + \Delta\varepsilon_i\left(\frac{\delta}{\delta_c}\right)^d \tag{4}$$

where $\Delta\varepsilon_{f0}$ is the inelastic failure strain range for an unoxidised coating system, δ_c is the critical oxide layer for which the coating would fail in a single cycle and c and d are constants which are $c \approx d \approx 1$. The oxide thickness can be expressed by a power-law equation, (see equation 1).

Model suggested by Busso et al.

Busso et al. have suggested the following model for APS TBCs, [61]:

$$\mathrm{d}D = D^m\left(\frac{\sigma_{\max}}{F}\right)^p \mathrm{d}N \tag{5}$$

where $0 \leqslant D \leqslant 1$ is a fatigue damage parameter such that $D = 1$ at failure, $\sigma_{\max}$ is the maximum out–of–plane interfacial stress, N is number of cycles and m and F are given by

$$m = 1 - C\left(\frac{\sigma_{\max}}{\sigma_{\mathrm{c0}}}\right)^{0.818p} \tag{6}$$

and

$$F = F_0\left(1 - F_1\sigma_{\max}\right) \tag{7}$$

where σ_{c0} is the initial strength and p, C, F_0 and F_1 are material parameters that need to be calibrated to experimental data.

The influence of high temperature phenomena is introduced by the calculation of $\sigma_{\max}$. The stress is obtained by finite element modelling which

includes effects such as oxidation and sintering, the finite element model is described in ref. [78]. Analytical functions are then fitted to the result of the finite element modelling, thus yielding closed-form expression of the maximum out–of–plane stress according to

$$\sigma_{\max} = \sigma_{\text{therm.}} + \sigma_{\text{ox.}} + \sigma_{\text{sintr.}} \tag{8}$$

where $\sigma_{\text{therm.}}$, $\sigma_{\text{ox.}}$, $\sigma_{\text{sintr.}}$ are functions of temperature, maximum temperature during cycling, cumulative oxidation time and BC/TC interface morphology; they describe the out–of–plane stress contributions from thermo-elastic and visco-plastic deformation, oxidation and sintering. These functions are given in ref. [61].

Model suggested by Brodin, Jinnestrand and Sjöström

The model put forward by Brodin, Jinnestrand and Sjöström, [56, 58, 79], is based on a Paris law type of expression:

$$\frac{dD}{dN} = C\left(\lambda \Delta G\right)^n \tag{9}$$

where G is the energy release rate and C and n are constants. D is a damage parameter according to

$$D = \frac{\sum_i l_i^{\text{TGO}} + \sum_j l_j^{\text{TC}} + \sum_k l_k^{\text{TC/TGO}}}{L} \tag{10}$$

where l_i^{TGO}, l_j^{TC} and $l_k^{\text{TC/TGO}}$ are the lengths of cracks running in the TGO, TC and TGO/TC interface respectively; L is the total analysed length.

This model assumes that the cracks partially, or completely, follow the TGO/TC interface; such a crack will grow in a mixed mode. To account for mixed mode cracks G is multiplied by a mixed mode function, λ, [80]:

$$\lambda = 1 - (1 - \lambda_0)\left(\frac{2}{\pi}\tan^{-1}\left(\frac{\Delta K_{II}}{\Delta K_I}\right)\right)^m \tag{11}$$

where ΔK_I and ΔK_{II} are the stress intensity factors in mode I and II, and λ_0 and m are constants.

The influence of thermal loads, surface morphology and interface TGO growth is included in the calculation of ΔG and $\Delta K_{\text{II}}/\Delta K_{\text{I}}$ in the following way: ΔG is first computed by a virtual crack extension method. From the finite element solution, also the crack flank displacements are taken. Using the theory of interface cracks, [80], these crack flank displacements can, in turn, be used for computing the relation $\Delta K_{\text{II}}/\Delta K_{\text{I}}$.

4

Experimental methods

4.1 Thermal fatigue

As the coefficient of thermal expansion differs between the bond coat and the top coat, stresses are introduced in the TBC system when thermally cycled. Two main types of thermal cycling tests exist: thermal cycling fatigue (TCF) (or furnace cycle test (FCT)) and burner rig test (BRT) (or thermal shock).

The burner rig test makes use of a flame to heat the specimen on the coated side; burner rigs typically reach a maximum gas temperature of 1350–1750 °C, [81]. Optionally, while heating, the specimens can be cooled on the uncoated side to introduce a larger temperature gradient in the specimen. After heating, the specimens are typically rapidly cooled by compressed air. Fig. 20 shows a schematic drawing of the burner rig used at Volvo Aero, Trollhättan; fig. 21 a) shows a typical BRT temperature curve. Burner rigs are used for a great variety of testing, such as: thermal shock, typically with short high temperature dwell time; oxidation tests with long dwell times; and hot corrosion tests, typically performed at temperatures around 900 °C, [81].

The furnace cycle test cycles the specimens between high and low temperature by moving them in and out of a resistance furnace. Such testing is associated witch notably lower heating rates than the burner rig test and the temperature gradients in the specimen are low; furthermore, the high temperature dwell time is usually longer compared to BRT. During cooling the specimens are often cooled by compressed air. Fig. 22 shows a schematic drawing of furnace cycling and fig. 21 b) shows a temperature curve.

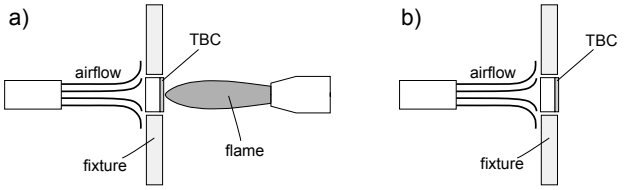

Figure 20: Schematic drawing of a burner rig. a) Heating by a flame at the coated side while cooling with air on the uncoated side. b) During the cold part of the cycle, the specimens are moved out of the flame and cooled at the uncoated side by air.

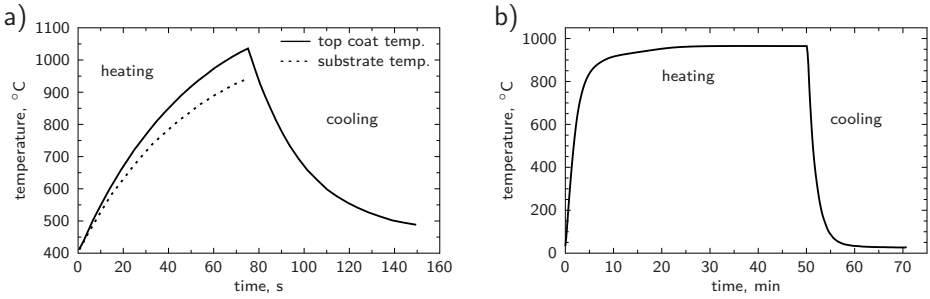

Figure 21: Example of two thermal cycles. a) A burner rig cycle where cooling (during the cold part of the cycle) has been done on the uncoated side, (based on ref. [73]). b) A furnace cycle with forced air cooling.

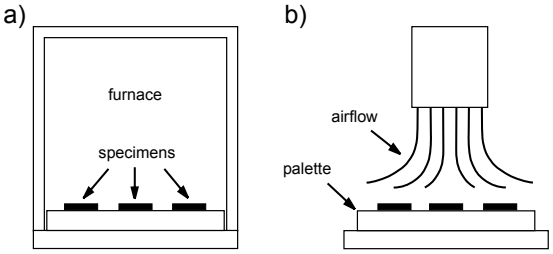

Figure 22: Schematic drawing of a cyclic furnace. a) Dwelling in furnace during the hot part of the cycle. b) Cooling with air during the cold part of the cycle.

4.2 Adhesion test

The tensile tests described in *ASTM C633 Standard test method for adhesion or cohesion strength of thermal spray coatings* and *EN 582 Thermal spraying – determination of tensile adhesive strength* offer simple approaches to adhesion assessments of TBCs. The method involves fastening the coated and uncoated sides of a button specimen to two bars that can be mounted in a tensile test machine, (equipped with universal joints to ensure moment free mounting); the set-up is schematically shown in fig. 23. The specimen is fastened to the bars by a suitable adhesive, most commonly by epoxy which is cured at moderate temperatures, (120–175 °C, [16]). During curing, a modest compressive load is applied to the bar/specimen/bar system to ensure good adhesion between fixture and specimen; a simple method for applying load, (which also ensures that the applied load is the same for all tested specimens), is by gravity bonding: letting the fixture/bar/fixture system stand upright during curing thereby being loaded with the force caused by the weight of the upper bar. Furthermore the specimens need to be flat and the surfaces need to be clean and free from loose material. The coating may therefore be ground or grit blasted. Furthermore, any coating overspray onto the sides of the button specimen, (as well as beads of excessive adhesive at the joint), must be removed before testing.

While the method enables the assessment of the adhesion strength of TBCs, some critical comments to the method are, [16]:

- Bending moments induced by mounting in the tensile test machine will give erroneous results. This is avoided by the use of a self aligning fixture, as shown in fig. 23, and by ensuring that the specimens are ground flat before adhesive bonding to the loading fixture.

- The type of adhesive will influence the result, as will the thickness of the adhesive film. In a porous coating, the penetration depth of the adhesive will effect the results. These effects stresses the importance of a consistent and repeatable curing procedure.

- The strength of the adhesive sets the upper limit for how strong coatings can be tested. Furthermore, the tensile test is unfit for evaluation of very thin and very porous coatings.

- Variation in coating thickness, distribution and size of defects in the coating and residual stresses may give scattered data.

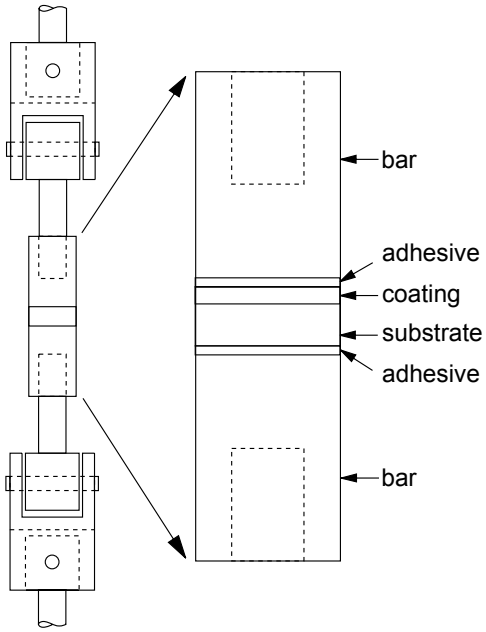

Figure 23: Experimental set-up for adhesion testing of TBCs, (image based on ref. [16]).

4.3 Interface roughness measurement

The BC/TC interface morphology can be measured and characterised on cross-sectioned specimens by the means of image analysis. A MATLAB script has been written which acquires the BC/TC interface roughness profile from grey-scale light–optic micrographs. The steps of the acquisition process are outlined in fig. 24; in short, the grey-scale images are made binary and the interface roughness profiles are obtained from the binary images. The interface roughness profiles are then used for calculation of various surface roughness parameters, the most well known probably being the profile arithmetic mean deviation:

$$\mathrm{P_a}, \mathrm{W_a}, \mathrm{R_a} = \frac{1}{l} \int_0^l |z(x)| \mathrm{d}x \tag{12}$$

where l is the analysed length and z and x are explained by fig. 24 c). The parameter is referred to as $\mathrm{P_a}$, $\mathrm{W_a}$ or $\mathrm{R_a}$ depending on how the measured profile has been filtered: $\mathrm{P_a}$ is the arithmetic mean deviation for an unfiltered profile while $\mathrm{W_a}$ and $\mathrm{R_a}$ refer to the arithmetic mean deviations for the long-wave and short-wave components of the profile. A comparison of $\mathrm{R_a}$ values, for some different surfaces, has shown that the $\mathrm{R_a}$ values obtained by image analysis are in good agreement with those obtained by a profilometer.

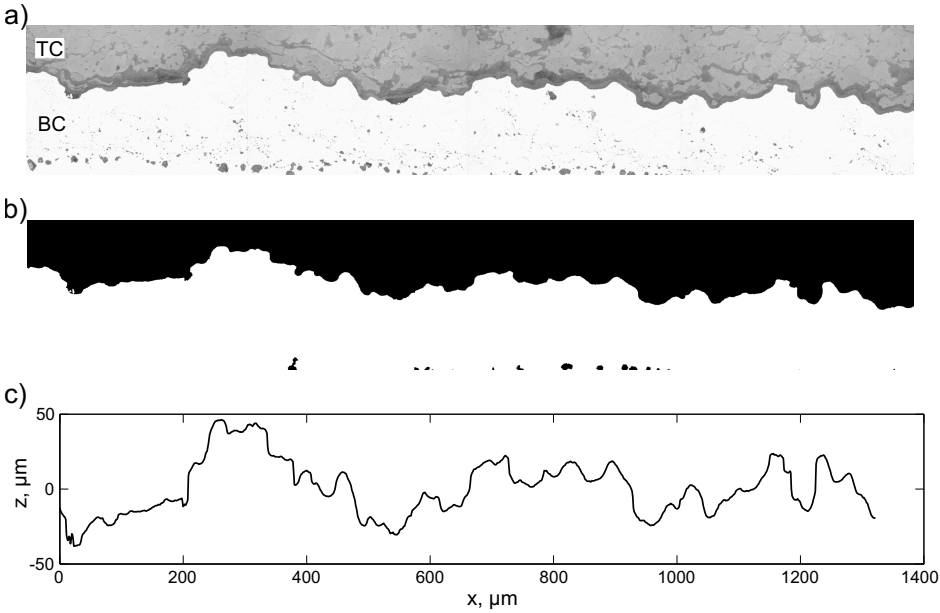

Figure 24: Interface roughness measurement by image analysis. a) Grey-scale light–optic micrograph. b) Binary image. c) Interface roughness profile.

5

Summary of appended papers

Paper I

Fracture mechanical modelling of a plasma sprayed TBC system

This paper studies the influence of BC/TC interface morphology on thermal fatigue life of TBCs. Four TBC systems, with varying BC/TC interface morphology, have been thermally cycled to failure and their fatigue lives have been correlated to their corresponding BC/TC interface roughness, W_a. The fatigue lives have also been calculated by the life model suggested by Brodin, Jinnestrand and Sjöström, (described in section 3.2.3), and a comparison between the experimental and theoretical results have been made. The specimens consist of Haynes 230 coupons coated with 200 µm of VPS NiCrAlY, (with 5 wt.% Al and additions of Si), and 350 µm of APS 7 wt.% Y-PSZ.

The results from the BC/TC interface roughness measurements show that a rougher interface increases the fatigue life of TBCs, (at least for the investigated range of interface roughness, W_a=7–11 µm). An increase in roughness from $W_a \approx 7$ µm to $W_a \approx 11$ µm gives an increase in fatigue life of ~ 70 %. In addition to the thermal fatigue tests, the specimens were also isothermally oxidised at 1100 °C for 1000 h. It was found that the BC/TC interface TGO thickness was ~ 10 µm for all specimens, regardless of interface roughness, thus showing that the differences in fatigue life were not due to differences in oxidation kinetics.

Modelling of the crack growth in the BC/TC interface was done for sinusoidal interfaces with roughness corresponding to 3, 6 and 10 µm. The modelling work predicts that the smoothest interface would have the longest life; this contradicts the experimental trend of longer life with increasing interface roughness. However, since the smoothest interface investigated experimen-

tally has an interface roughness of $W_a \approx 7\,\mu m$, the actual roughness–life relation is not known for as smooth interfaces as $W_a = 3\,\mu m$. For the two roughest interfaces, the $W_a = 10\,\mu m$ interface is predicted to give longer life than the interface with $W_a = 6\,\mu m$; this correlates with the experimental findings.

The paper clearly depicts the large influence of BC/TC interface roughness on the fatigue life of TBCs. Further work in this area is necessary in order to accurately model the BC/TC interface morphology. It should be noted that this paper only deals with the influence of different sine wave amplitudes. A variation of the sine wave wavelength will also influence the predicted life. However, the W_a interface roughness parameter cannot capture the influence of different wavelengths and alternative roughness parameters should be investigated.

Paper II

Influence of isothermal and cyclic heat treatments on the adhesion of plasma sprayed thermal barrier coatings

This paper studies the influence of a few different heat treatments on the adhesion properties of thermal barrier coatings. The studied TBC system consists of Hastelloy X as base material coated with an air plasma sprayed NiCoCrAlY bond coat, ($\sim 12\,$wt.% Al), and air plasma sprayed 7 wt.% Y-PSZ as top coat. The coated specimens have been heat treated at a temperature of $\sim 1100\,^{\circ}$C by isothermal oxidation, furnace cycling and burner rig cycling. The adhesion tests have been made by the method described in the ASTM standard *ASTM C633: Standard test method for adhesion or cohesion strength of thermal spray coatings*.

Due to the relatively low cumulative high temperature exposure associated with the burner rig test, these specimens only developed a thin layer of interface TGO which consisted mainly of Al_2O_3; the interdiffusion of Al with the substrate was very modest and the microstructure of the bond coat contained the Al-rich β-phase throughout the testing. The isothermal oxidation and furnace cycling gave thicker interface TGOs which, in addition to Al_2O_3, contained $(Cr, Al)_2O_3$, NiO and spinels for long high temperature oxidation times.

The adhesion of the TBC was tested for the heat treated specimens, as well as for an as-sprayed specimen. The adhesion of the isothermally heat treated specimens increased about 50 % compared to the as-sprayed condition and the adhesion were found to increase slightly with oxidation

time. Possible explanations for this are: the relaxation of residual stresses, sintering and beneficial effects of a thin layer of BC/TC interface TGOs.

The adhesion of the two cyclic heat treatments decreased with time, which is attributed to the fatigue damage introduced in the specimens during cycling. In the case of burner rig testing, however, no substantial cracking was found by light–optic microscopy. The burner rig test gives a slower decrease of adhesion with number of cycles: $\sim 1.54 \cdot 10^{-3}$ MPa/cycle, compared with $\sim 20.44 \cdot 10^{-3}$ MPa/cycle for furnace cycling. This appears to be consistent with the tendency for longer high temperature dwell times to reduce the number of cycles to failure, as reported by, for example, ref. [82].

Paper III

Fractographic and microstructural study of isothermally and cyclically heat treated thermal barrier coatings

This paper includes a fractographic study emphasising the differences found on fracture surfaces of adhesion tested TBC systems exposed to a few different heat treatments. The paper also includes a study of microstructural changes in the top coat due to high temperature exposure. The studied TBC system consists of a Hastelloy X substrate coated with air plasma sprayed NiCoCrAlY, ($\sim$ 12 wt.% Al), and air plasma sprayed 7 wt.% Y-PSZ. The coated specimens have been heat treated at a temperature of $\sim$ 1100 °C by isothermal oxidation, furnace cycling and burner rig cycling. The top coats have been torn off the specimens by an adhesion test set-up using a tensile test machine.

The fracture was found to occur mainly in the top coat. Isothermal heat treatment gave fracture almost entirely in the top coat while the two cyclic heat treatments gave increasing BC/TC interface fracture with number of cycles, but still > 80 % of the fracture occurred in the top coat. The parts of the fracture surfaces where fracture occurred in the top coat showed essentially the same characteristics regardless of heat treatment: the fracture occurred mainly between the splats in the, for plasma spraying, typical splat–on–splat structure; extensive through–splat fracture occurred only sparingly and always associated with discontinuities in the microstructure, such as partially melted particles.

The cyclic heat treatments gave some BC/TC fracture, thus enabling a study of the interface TGOs. For specimens subjected to furnace cycling, the exposed TGOs were clearly cracked while burner rig tested specimens had an intact layer of TGOs. Furthermore, the furnace cycled specimens had TGOs

that consisted of chromia and spinels. These oxides are occasionally found in clusters containing chromia, spinels and nickel oxide. Such oxide clusters are often cut-through during fracture.

This paper illuminates several of the degrading mechanisms that occur in TBCs at high-temperature exposure and thermal cycling: introduction of fatigue damage, interface TGO growth, grain coarsening and sintering of the top coat. In particular, the paper shows the difference between isothermal and cyclic heat treatment. While the isothermal oxidation gives white fracture, cyclic heat treatments give increasing fractions of black fracture with number of cycles.

Paper IV

Fractographic study of adhesion tested thermal barrier coatings subjected to isothermal and cyclic heat treatments

This conference paper relies on the same experimental results as those already presented in paper II and III, but adds to the discussion by contrasting the fracture mechanisms in TCF- and BRT-subjected specimens.

While both TCF and BRT increases the amount of black fracture, the damage mechanisms are somewhat different. In the case of TCF, cycling clearly introduces BC/TC interface damage; cracked interface TGO can be seen both on cross-sections and fracture surfaces. The increasing amount of black fracture can therefore be attributed to an increase in interfacial damage. For BRT, however, no interfacial damage can be seen for up to 1150 cycles on cross-sections or fracture surfaces; the thin layer of interface TGOs remains uncracked throughout testing.

6

Conclusions

The presented research includes studies of high-temperature degradation mechanisms, as well as a study on the influence of bond coat/top coat interface morphology on the fatigue life of TBCs. The presented results will be important in the continuing life prediction work which will, in the long run, contribute to higher reliability of TBC systems in gas turbines.

The influence of bond coat/top coat interface morphology has been shown to influence fatigue life of TBCs. It has also been shown that finite element modelling of crack growth in the bond coat/top coat depends heavily on the choice of modelled bond coat/top coat interface geometry.

Three common high temperature testing methods for TBCs, (isothermal oxidation, furnace cycle test and burner rig test), have been compared. Isothermal oxidation was shown to have beneficial effects on the adhesion properties of TBCs, while burner rig test and furnace cycling both lowered the adhesion strength. The burner rig test gives lower adhesion strength but slower decrease in adhesion.

The fracture during adhesion testing of TBCs has been found to follow pre-existing defects in the top coat. Isothermal and cyclic heat treatment were found to promote different failure mechanisms: isothermal oxidation gives fracture in the top coat while thermal cycling promotes bond coat/top coat fracture. Furnace cycling results in a clearly cracked interface TGO while the burner rig test leaves the TGO essentially intact.

Acknowledgement

This research has been funded by the Swedish Energy Agency, Siemens Industrial Turbomachinery AB, Volvo Aero Corporation, and the Royal Institute of Technology through the Swedish research programme TURBO POWER, the support of which is gratefully acknowledged.

In addition, I would like to thank the group of skilled researchers and engineers that I have had the pleasure of working with during these past years: Sten Johansson, Håkan Brodin, Sören Sjöström, Lars Östergren and Xin-Hai Li.

I would also like to thank Jan Kanesund for providing the SEM image of Inconel 792 in fig. 4 a) and Kang Yuan for helping out with the THERMO-CALC calculations in fig. 7.

Bibliography

[1] D. Stöver and C. Funke. Directions of the development of thermal barrier coatings in energy applications. *J. Mater. Process. Technol.*, 92-93:195–202, 1999.

[2] D.M. Comassar. Surface coatings technology for turbine engine applications. *Met. Finish.*, 89(3):39–44, 1991.

[3] M. Belmonte. Advanced ceramic materials for high temperature applications. *Adv. Eng. Mater.*, 8(8):693–703, 2006.

[4] R.A. Miller. Thermal barrier coatings for aircraft engines: history and directions. *J. Therm. Spray Technol.*, 6(1):35–42, 1997.

[5] J.T. DeMasi-Marcin and D.K. Gupta. Protective coatings in the gas turbine engine. *Surf. Coat. Technol.*, 68–69:1–9, 1994.

[6] C.T. Sims, N.S. Stoloff, and W.C. Hagel, editors. *Superalloys II.* Wiley-intersience, 1987.

[7] J.R. Davis, editor. *Heat-Resistant Materials.* ASM International, 1999.

[8] R. C. Reed. *The superalloys: fundamentals and applications.* Cambridge University Press, 2006.

[9] H.E. Evans and M.P. Taylor. Oxidation of high-temperature coatings. *Proc. IMechE*, 220(G):1–10, 2006.

[10] S. Bose. *High Temperature Coatings.* Butterworth-Heinemann, 2007.

[11] C. G. Levi. Emerging materials and processes for thermal barrier systems. *Curr. Opin. Solid State Mater. Sci.*, 8:77–91, 2004.

[12] R. Mévrel. State of the art on high-temperature corrosion-resistant coatings. *Mater. Sci. Eng., A*, 120:13–24, 1989.

[13] K.K. Gupta, A. Rehman, and R.M. Sarviya. Bio-fuels for the gas turbine: a review. *Renew. Sustain. Energy Rev.*, 14:2946–2955, 2010.

[14] W.A. Nelson and R.M. Orenstein. TBC experience in land-based gas turbines. *J. Therm. Spray Technol.*, 6(2):176–180, 1997.

[15] A.K. Ray and B. Goswami. Applications of thermal barrier coating system in gas turbines – a review. *J. Metall. Mater. Sci.*, 46(1):1–22, 2004.

[16] J.R. Davis, editor. *Handbook of thermal spray technology.* ASM International, 2004.

[17] X. Zhao and P. Xiao. Thermal barrier coatings on nickel superalloy substrates. *Mater. Sci. Forum*, 606:1–26, 2009.

[18] L.B. Chen. Yttria-stabilized zirconia thermal barrier coatings – a review. *Surf. Rev. Lett.*, 13(5):535–544, 2006.

[19] X.Q. Cao, R. Vaßen, and D. Stöver. Ceramic materials for thermal berrier coatings. *J. Eur. Ceram. Soc.*, 24:1–10, 2004.

[20] S. Stecura. Optimization of the Ni–Cr–Al–Y/ZrO_2–Y_2O_3 thermal barrier system. *Adv. Ceram. Mater.*, 1(1):68–76, 1986.

[21] J. A. Haynes, M. K. Ferber, W. D. Porter, and E. D. Rigney. Characterization of alumina scales formed during isothermal and cyclic oxidation of plasma-sprayed TBC systems at 1150 °C. *Oxid. Met.*, 52(1–2):31–76, 1999.

[22] C. Burman. *Properties of plasma sprayed FeCrAlY coatings on high temperature alloys.* PhD thesis, Linköpings universitet, 1986.

[23] H. Hindam and D.P. Whittle. Microstructure, adhesion and growth kinetics of protective scales on metals and alloys. *Oxid. Met.*, 18(5–6): 245–284, 1982.

[24] P. Choquet, C. Indrigo, and R. Mévrel. Microstructure of oxide scales formed on cyclically oxidized M–Cr–Al–Y coatings. *Mater. Sci. Eng.*, 88:97–101, 1987.

[25] K. Ma and J.M. Schoenung. Thermodynamic investigation into the equilibrium phases in the NiCoCrAl system at elevated temperatures. *Surf. Coat. Technol.*, 205:2273–2280, 2010.

[26] M.M. Morra, R.R. Biederman, and R.D. Sisson JR. Microstructural characterization of metallic overlay coatings by high resolution analytical electron microscopy. *Thin Solid Films*, 119:383–394, 1984.

[27] B.G. Mendis, B. Tryon, and T.M. Pollock andf K.J. Hemker. Microstructural observations of as-prepared and thermal cycled NiCoCrAlY bond coats. *Surf. Coat. Technol.*, 201:3918–3925, 2006.

[28] B. Baufeld and M. Schmücker. Microstructural evolution of a NiCoCrAlY coating on an IN100 substrate. *Surf. Coat. Technol.*, 199:49–56, 2005.

[29] D.R.G. Achar, R. Munoz-Arroyo, L. Singheiser, and W.J. Quadakkers. Modelling of phase equilibria in MCrAlY coating systems. *Surf. Coat. Technol.*, 187:272–283, 2004.

[30] W. Brandl, H.J. Grabke, D. Toma, and J. Kruger. The oxidation behaviour of sprayed MCrAlY coatings. *Surf. Coat. Technol.*, 86-87:41–47, 1996.

[31] EN 657: Thermal spraying – terminology, classification.

[32] M. Friis, C. Persson, and J. Wigren. Influence of particle in-flight characteristics on the microstructure of atmospheric plasma sprayed yttria stabilized ZrO_2. *Surf. Coat. Technol.*, 141:115–127, 2001.

[33] H. Liu, H.R. Salimi Jazi, M. Bussmann, and J. Mostaghimi. Experiments and modeling of rapid solidification of plasma-sprayed yttria-stabilized zirconia. *Acta Mater.*, 57:6013–6021, 2009.

[34] A. Nusair Khan, J. Lu, and H. Liao. Heat treatment of thermal barrier coatings. *Mater. Sci. Eng., A*, 359:129–136, 2003.

[35] P. Bengtsson. *Microstructural, Residual Stress and Thermal Shock Studies of Plasma Sprayed ZrO_2-based Thermal Barrier Coatings.* PhD thesis, Linköpings universitet, 1997.

[36] N. Markocsan, P. Nylén, J. Wigren, X.-H. Li, and A. Tricoire. Effect of thermal aging on microstructure and functional properties of zirconia-base thermal barrier coatings. *J. Therm. Spray Technol.*, 18(2):201–208, 2009.

[37] R. McPherson. A review of microstructure and properties of plasma sprayed ceramic coatings. *Surf. Coat. Technol.*, 39–40:173–181, 1989.

[38] C.S. Giggins and F.S. Pettit. Oxidation of Ni–Cr–Al alloys between 1000 °C and 1200 °C. *J. Electrochem. Soc.*, 118(11):1782–1790, 1971.

[39] J. A. Haynes, E. D. Rigney, M. K. Ferber, and W. D. Porter. Oxidation and degradation of a plasma-sprayed thermal barrier coating system. *Surf. Coat. Technol.*, 86–87:102–108, 1996.

[40] W.G. Sloof and T.J. Nijdam. On the high-temperature oxidation of MCrAlY coatings. *Int. J. Mat. Res.*, 100(10):1318–1330, 2009.

[41] R. Prescott and M.J. Graham. The formation of aluminum oxide scales on high-temperature alloys. *Oxid. Met.*, 38(3–4):233–254, 1992.

[42] F.H. Stott, G.C. Wood, and J. Stringer. The influence of alloying elements on the development and maintenance of protective scales. *Oxid. Met.*, 44(1–2):113–145, 1995.

[43] C. Wagner. Contributions to the theory of the tarnishing process. *Z. Phys. Chem.*, B21:25–41, 1933.

[44] W.J. Quadakkers, D. Naumenko, E. Wessel, V. Kochubey, and L. Singheiser. Growth rates of alumina scales on Fe–Cr–Al alloys. *Oxid. Met.*, 61(1–2):17–37, 2004.

[45] P. Niranatlumpong, C.B. Ponton, and H.E. Evans. The failure of protective oxides on plasma-sprayed NiCoCrAlY overlay coatings. *Oxid. Met.*, 53(3–4):241–258, 2000.

[46] D. Naumenko, B. Gleeson, E. Wessel, L. Singheiser, and W.J. Quadakkers. Correlation between the microstructure, growth mechanism, and qrowth kinetics of alumina scales on a FeCrAlY alloy. *Metall. Mater. Trans. A*, 38A:2974–2983, 2007.

[47] G.R. Wallwork and A.Z. Hed. The oxidation of Ni–20 wt.% Cr–2ThO_2. *Oxid. Met.*, 3(3):229–241, 1971.

[48] C. Wagner. Passivity and inhibition during the oxidation of metals at elevated temperatures. *Corr. Sci.*, 5:751–764, 1965.

[49] G.R. Wallwork and A.Z. Hed. Some limiting factors in the use of alloys at high temperatures. *Oxid. Met.*, 3(2):171–184, 1970.

[50] W.R. Chen, X. Wu, B.R. Marple, and P.C. Patnaik. Oxidation and crack nucleation/growth in an air-plasma-sprayed thermal barrier coating with NiCrAlY bond coat. *Surf. Coat. Technol.*, 197:109–115, 2005.

[51] D. Renusch, M. Schorr, and M. Schütze. The role that bond coat depletion of aluminum has on the lifetime of APS-TBC under oxidizing conditions. *Mater. Corr.*, 59(7):547–555, 2008.

[52] H.E. Evans and M.P. Taylor. Diffusion cells and chemical failure of MCrAlY bond coats in thermal-barrier coating systems. *Oxid. Met.*, 55 (1–2):17–34, 2001.

[53] H.E. Evans, A.T. Donaldson, and T.C. Gilmour. Mechanisms of breakaway oxidation and application to a chromia-forming steel. *Oxid. Met.*, 52(5–6):379–402, 1999.

[54] W.R. Chen, X. Wu, B.R. Marple, D.R. Nagy, and P.C. Patnaik. TGO growth behaviour in TBCs with APS and HVOF bond coats. *Surf. Coat. Technol.*, 202:2677–2683, 2008.

[55] E.A.G. Shillington and D.R. Clarke. Spalling failure of a thermal barrier coating associated with aluminum depletion in the bond-coat. *Acta Mater.*, 47(4):1297–1305, 1999.

[56] H. Brodin. *Failure of thermal barrier coatings under thermal and mechanical fatigue loading: Microstructural observations and modelling aspects.* PhD thesis, Linköpings universitet, 2004.

[57] M.S. Ali, Shenhua Song, and Ping Xiao. Degradation of thermal barrier coatings due to thermal cycling up to 1150 °C. *J. Mater. Sci.*, 37:2097–2102, 2002.

[58] M. Jinnestrand. *Delamination in APS applied thermal barrier coatings: life modelling.* PhD thesis, Linköpings universitet, 2004.

[59] P. Bednarz. *Finite element simulation of stress evolution in thermal barrier coating systems.* PhD thesis, RWTH Aachen University, 2006.

[60] M. Jinnestrand and S. Sjöström. Investigation by 3D FE simulations of delamination crack initiation in TBC caused by alumina growth. *Surf. Coat. Technol.*, 135:188–195, 2001.

[61] E.P. Busso, J. Lin, and S. Sakurai. A mechanistic study of oxidation-induced degradation in a plasma sprayed thermal barrier coating system. part II: life prediction model. *Acta Mater.*, 49:1529–1536, 2001.

[62] A. Rabiei and A.G. Evans. Failure mechanism associated with the thermally grown oxide in plasma-sprayed thermal barrier coatings. *Acta Mater.*, 48:3963–3976, 2000.

[63] R. Vaßen, G. Kerkhoff, and D. Stöver. Development of a micromechanical life prediction model for plasma sprayed thermal barrier coatings. *Mater. Sci. Eng., A*, 303:100–109, 2001.

[64] F. Traeger, M. Ahrens, R. Vaßen, and D. Stöver. A life model for ceramic thermal barrier coatings. *Mater. Sci. Eng., A*, 358:255–265, 2003.

[65] W.R. Chen, X. Wu, B.R. Marple, and P.C. Patnaik. The growth and influence of thermally grown oxide in a thermal bearrier coating. *Surf. Coat. Technol.*, 201:1074–1079, 2006.

[66] W.R. Chen, X. Wu, B.R. Marple, R.S. Lima, and P.C. Patnaik. Preoxidation and TGO growth behaviour of an air-plasma-sprayed thermal barrier coating. *Surf. Coat. Technol.*, 202:3787–3796, 2008.

[67] D. Naumenko, V. Shemet, L. Singheiser, and W.J. Quadakkers. Failure mechanisms of thermal berrier coatings on MCrAlY-type bondcoats associated with the formation of the thermally grown oxide. *J. Mater. Sci.*, 44:1687–1703, 2009.

[68] F. Tang and J.M. Schoenung. Local accumalation of thermally grown oxide in plasma-sprayed thermal barrier coatings with rough topcoat/bond-coat interfaces. *Scr. Mater.*, 52:905–909, 2005.

[69] K.W. Schlichting, N.P. Padture, E.H. Jordan, and M. Gell. Failure modes in plasma-sprayed thermal barrier coatings. *Mater. Sci. Eng., A*, 342:120–130, 2003.

[70] H. Echsler, V. Shemet, M. Schütze, L. Singheiser, and W.J. Quadakkers. Cracking in and around the thermally grown oxide in thermal barrier coatings: A comparison of isothermal and cyclic oxidation. *J. Mater. Sci.*, 41:1047–1058, 2006.

[71] H. Echsler, D. Renusch, and M. Schütze. Bond coat oxidation and its significance for life expectancy of thermal barrier coating systems. *Mater. Sci. Technol.*, 20:307–318, 2004.

[72] S. Sjöström and H. Brodin. Influence of TBC end geometry on the TMF life of an APS TBC. *Procedia Eng.*, 2:1363–1371, 2010.

[73] Y. Liu, C. Persson, and J. Wigren. Experimental and numerical life prediction of thermally cycled thermal barrier coatings. *J. Therm. Spray Technol.*, 13(3):415–424, 2004.

[74] E.Y. Lee, D.M. Chartier, R.R. Biederman, and R.D. Sisson JR. Modelling the microstructural evolution and degradation of the M–Cr–Al–Y coatings during high temperature oxidation. *Surf. Coat. Technol.*, 32: 19–39, 1987.

[75] J.A. Nesbitt and R.W. Heckel. Modeling degradation and failure of Ni–Cr–Al overlay coatings. *Thin Solid Films*, 119:281–290, 1984.

[76] J.A. Nesbitt, EE.J. Vinarcik, C.A. Barrett, and J. Doychak. Diffusional transport and predicting oxidative failure during cyclic oxidation of β-NiAl alloys. *Mater. Sci. Eng., A*, 153:561–566, 1992.

[77] J.T. DeMasi, K.D. Sheffler, and M. Ortiz. Thermal barrier coating life prediction model development, phase I – final report. Technical report, Nasa-CR-182230, 1989.

[78] E.P. Busso, J. Lin, S. Sakurai, and M. Nakayama. A mechanistic study of oxidation-induced degradation in a plasma sprayed thermal barrier coating system. part I: model formulation. *Acta Mater.*, 49:1515–1528, 2001.

[79] S. Sjöström and H. Brodin. Thermomechanical fatigue life of TBCs – experimental and modelling aspects. In *Ceramic Engineering and Science Proceedings*, 2010.

[80] J.W. Hutchinson and Z. Suo. *Advances in applied mechanics*, chapter Mixed mode cracking in layered materials, pages 63–192. Academic press, 1992.

[81] R. Vaßen, F. Cernushi, G. Rizzi, A. Scrivani, N. Markocsan, L. Östergren, A. Kloosterman, R. Mevrel, J. Feist, and J. Nicholls. Recent activities in the field of thermal barrier coatings including burner rig testing in the european union. *Adv. Eng. Mater.*, 10:907–921, 2008.

[82] O. Trunova, T. Beck, R. Herzog, R. W. Steinbrech, and L. Singheiser. Damage mechanisms and lifetime behavior of plasma sprayed thermal barrier coating systems for gas turbines – part I: Experiments. *Surf. Coat. Technol.*, 202:5027–5032, 2008.